fold compared to that of wild-type AChR, indicating an increased affinity of ACh for one or more of the closed, open or desensitized states of the mutant receptor (data not shown).

Activation kinetics of the δL42P mutant. To determine whether the mutations affect the kinetics of AChR activation, we recorded single channel currents elicited by a low concentration of ACh from HEK cells expressing wild-type, δL42P, and δV93L AChRs. At a concentration of 50 nM ACh, channel openings of di-liganded AChRs appear in bursts of several openings in quick succession and provide an indirect measure of the decay rate of post-synaptic currents. Burst duration histograms of δL42P AChR displayed two components whereas those of wild-type and the other mutant AChRs displayed three components (Figure 4). The mean duration of the longest component of bursts for the δL42P receptor was 0.76 ms, much briefer than the corresponding value of 3.3 ms for the wild type AChR, while that of the δV93L receptor was mildly but significantly prolonged (Table 3). Because δI58K is essentially a null mutation and δV93L is not pathogenic, δL42P determines the phenotype.

To determine the mechanism by which the δL42P mutant shortens bursts of channel openings, we examined the activation kinetics of the δL42P mutant AChR by recording single channel currents over a range of ACh concentrations (see Experimental Methods). For both wild type and δL42P AChRs, the distributions of closed durations exhibited several exponential components that shifted from long to brief durations with increasing ACh concentrations (Fig. 5A, B). However for the δL42P mutant AChR, the shift toward brief durations was significantly less, and at a saturating concentration of ACh, closed durations remained prolonged. Open durations for the δL42P mutant changed little across the range of ACh concentrations and were uniformly briefer than observed for the wild type AChR.

To quantify changes in elementary rate constants underlying activation of the mutant AChR, we fitted Scheme 1 (Fig. 6) to the single channel closed and open intervals elicited by the entire range of ACh concentrations displayed in Fig. 5. The scheme depicts AChR activation as the reversible binding of two agonists (A) to AChRs in the closed state (R) followed by reversible formation of the open state (R*). At high concentrations, the agonist blocks the open channel to form the blocked state (R_B).

For both wild type and δL42P mutant AChRs, Scheme 1 describes the dwell time distributions over the entire range of ACh concentrations, as shown by the smooth curves overlying the histograms. The analysis gives estimates of rate constants for ACh association and dissociation and opening and closing of the channel (Table 4). The most significant effect of δL42P is a 12.5-fold decrease of the di-liganded channel gating equilibrium constant θ_2, which results from a decrease of the channel opening rate constant β_2 and an increase of the channel closing rate constant α_2. Elementary steps for ACh binding were modestly affected by the mutation, with rate constants for ACh dissociation, k_{-1} and k_{-2}, slowed; although the estimate of k_{-2} was well-defined, the estimate of k_{-1} showed a larger error and thus greater uncertainty.

The fitted rate constants account quantitatively for the dependence of channel open probability (P_{open}) on ACh concentration, showing that δL42P shifts P_{open} to lower ACh concentrations and decreases its maximum (Fig. 5C). Furthermore the burst duration, approximated by $(1 + \beta_2/k_{-2})/\alpha_2$, predicts a value of 0.7 ms which agrees closely with the independently determined burst duration of 0.76 ms recorded with 50 nM ACh (Table 3); both values predict abnormally fast decay of synaptic currents typical of the fast-channel CMS. The probability a di-liganded channel will open following a pulse of nerve-released ACh, given by

$\beta_2/(\beta_2 + k_{-2})$, decreases from 0.84 for the wild type AChR to 0.53 for the δL42P mutant AChR, predicting a reduced peak synaptic response.

Other substitutions of δL42. δL42P introduces a proline residue in the lower third of the β_1 strand (Figure 7A) which could destabilize the anti-parallel inner β-sheet by breaking inter-strand hydrogen bonds. To determine whether the mutation effects are proline-specific, we introduced into δ codon 42 the small and flexible residue Gly as well as the charged residues Lys and Asp. Each of these mutations generated abnormally brief channel bursts (Table 3) and reduced the channel gating equilibrium constant 12- to 25-fold, mainly by slowing β_2 (Table 4). Thus the attenuated gating by δL42P is not proline-specific and not due to disruption of hydrogen bonds; the effects may instead result from a local structural disturbance of the subunit interface or the hydrophobic core of the δ subunit.

Proline substitution in other subunits of residues aligning with δL42. To determine whether the effects of δL42P are subunit specific, we mutated the corresponding Leu in the ε, β, and α subunits to Pro. Compared to wild-type AChR, εL40P decreases the burst duration by ~50% (Figure 4 and Table 3), reduces P_{open} to a lesser extent than δL42P (Fig. 5C), and attenuates the channel gating equilibrium constant 4-fold (Table 4). βL40P decreases the burst duration by 30% (Table 3), but affects neither P_{open} (Fig. 5C) nor the gating equilibrium constant (Table 4). In striking contrast to mutations in the β-, δ- and ε-subunits, mutation of the equivalent residue in the α-subunit αL40P prolongs the longest component of opening bursts ~4 fold (Figure 4 and Table 3). The overall results indicate that the lower β_1 strands of the different subunits contribute to AChR activation in distinct and in some cases opposing ways.

Proline mutations of residues adjacent to δL42. To determine whether the effects of the mutation are specific to the location of δL42P within the β_1 strand, we performed proline

scanning mutagenesis two residues upstream and downstream of δL42. We found that δN41P, δI43P, and δS44P decreased the major long component of bursts to 0.6-0.71 ms, like δL42P, and δS40P decreased it to 0.35 ms (Table 3). Thus, over a span of four consecutive residues within the β_1 strand of the δ-subunit, substitution of proline attenuates receptor activation.

Mutant cycle analysis. δL42 and the equivalent εL40 are located at subunit interfaces, suggesting they contribute to channel gating affecting interaction between the subunits. Moreover, previous mutant cycle analyses revealed that the adjacent residues, δN41 and εN39, couple energetically with the proximal αY127 from the juxtaposed α-subunit (13). We therefore used mutant cycle analyses (16) to determine whether δL42 and εL40 also couple energetically with αY127. Using $-RT\ln\theta_2$ the free energy of channel gating of each mutant AChR, we generated a 2-dimensional mutant cycle composed of gating equilibria for wild type, δL42P/εL40P, αY127T and αY127T/δL42P/εL40P AChRs (Fig. 7). The resulting inter-residue coupling free energy of 3.9 kcal/mol is large and approaches the value of 5.8 kcal/mol obtained for the previously described mutant cycle generated using the mutations αY127T, δN41A and εN39A.

To determine the origin of the coupling energy, we cast three more 2-dimensional mutant cycles using subsets of the three residue substitutions. The mutant cycles αY127/δL42P and αY127/εL40P exhibit approximately equal coupling free energies approaching 2 kcal/mol, showing that at the two subunit interfaces, the residue pairs contribute equally to the overall coupling energy. The mutant cycle δL42P/εL40P reveals a low coupling energy of 0.7 kcal/mol, indicating δL42P and εL40P, which are far apart in the 3D structure, are essentially independent in contributing to gating. Thus although δL42P and εL40P are independent of each other, their contributions to channel gating depend on the juxtaposed αY127 of the neighboring α-subunit.

Discussion

We identify three mutations in β strands of the AChR δ subunit in a patient with moderately severe to severe myasthenic symptoms since birth. One mutation, δV93L has no appreciable kinetic affects and allows for robust AChR expression in HEK cells. The second mutation on the same allele, δI58K, hinders δ/α subunit association and is essentially a null mutation. Hence the third mutation, δL42P, determines the phenotype. Although this mutation modestly enhances affinity of the di-liganded closed receptor, it decreases the gating efficiency of the diliganded receptor 13-fold, and reduces AChR expression in HEK cells to 37% of wild-type. The activation rate constants of the δL42P-receptor in Table 4 predict a mean burst duration of 0.7 ms, close to that measured for bursts elicited by a low ACh concentration (Table 3). This value predicts a 5-fold faster decay of synaptic currents at patient than at normal EPs. The activation rate constants also predict that channel opening probability during synaptic transmission is decreased from 0.84 to 0.53; thus only ~60% of the synaptic AChRs would be opened by an instantaneous pulse of ACh. The amplitude of the synaptic response is additionally curtailed by reduced expression of the δL42P-AChR, and by the simplified junctional folds which decrease (17). Thus, the safety margin of neuromuscular transmission is compromised by the combined effects of EP AChR deficiency, reduced opening probability of the available receptors, and abnormally fast decay of the synaptic current.

We also find that the consequences δL42P are not Pro specific, because substitution with a charged Asp or Lys, or with a small and flexible Gly, has similar kinetic effects. Pro mutants at δN41, δI43, and δS44 mimic the effects of δL42P, indicating that a span of 4 residues in the β1 strand of the δ subunit is critical for maintaining gating efficiency. Mutation of residues that align with δL42 in the ε, β, and α-subunit impede, fail to alter, or enhance gating; therefore the

effects of the mutation are subunit specific. Finally, using mutant cycle analysis we show that δL42 and εL40 contribute to an inter-subunit linkage required for efficient channel gating. The patient mutation likely causes a local structural perturbation that alters the primary inter-subunit linkage between δN41, adjacent to the patient mutation, and the juxtaposed αY127.

Although the identified Leu in the β1 strand is conserved at equivalent positions of the α, β, ε and δ-subunits, the contributions of the Leu to AChR activation depend on the subunit. Differences in residues proximal to the identified Leu may therefore contribute to the different functional consequences of the mutations. The Leu in the δ and ε subunits is adjacent to the key Asn residue that spans the subunit interface and mediates inter-subunit interactions with αY127 required for efficient channel gating. None of the other subunit interfaces contain the Tyr/Asn linkage, suggesting inter-subunit interactions at the α-δ and α-ε interfaces contribute uniquely to channel gating. Before the current study, it was not known whether residues at equivalent positions of the other three subunit interfaces mediate inter-subunit interactions that contribute to channel gating. However by examining the equivalent Leu in the α-subunit, we find that two interfaces, ε-α and β-α, contribute to channel gating but in a novel manner. Structural perturbation of these interfaces by the mutation αL40P enhances rather than attenuates channel gating. Thus residue differences at these interfaces, whether proximal or distal to αL40, emerge as candidates for inter-subunit linkages mediating global communication required for channel gating.

Methods

Muscle specimens. Intercostal muscle specimens were obtained intact from origin to insertion from patients and control subjects without muscle disease undergoing thoracic surgery. All human studies were in accord with the guidelines of the Institutional Review Board of the Mayo Clinic.

AChR and acetylcholinesterase were detected in cryostat sections by two-color fluorescence (18). Endplates (EPs) were localized for electron microscopy and analyzed by the established methods (19). Peroxidase-labeled α-bgt was used for the ultrastructural localization of AChR (20). The number of AChRs per EP was measured with [^{125}I]α-bungarotoxin (α-bgt) (21).

Electrophysiology of muscle specimens. Recordings of EP potentials and currents (EPCs) and estimates of the number of transmitter quanta released by nerve impulse were performed as described elsewhere (21, 22), except that the amplitude of the miniature EP potentials (MEPPs) and currents (MEPCs) were estimated from the quantal components of the EPP and EPC, respectively (23).

Mutation analysis. We directly sequenced AChR α, β, δ, and ε subunit genes using genomic DNA. The mutations were traced with allele-specific PCR in family members and in 200 normal alleles of 100 unrelated controls.

Construction and expression of wild-type and mutant AChRs. Sources of human α, β, ε and δ subunit cDNAs were as previously described (24). All four cDNAs were subcloned into the CMV-based expression vector pRBG4 for expression in human embryonic kidney fibroblast (293 HEK) cells (24). The artificial mutations were engineered into wild-type AChR subunit cDNAs in pRBG4 using the QuikChange Site-Directed Mutagenesis Kit (Stratagene). The presence of each mutation and absence of unwanted mutations was confirmed by sequencing the entire inserts. HEK

cells were transfected with plasmids comprising of pRBG4-α, -β, -δ, -ε, and pEGFP-N1 in a ratio of 2:1:1:1:1 using FuGene6 transfection reagent (Roche).

α-Bungarotoxin binding measurements. The total number of [^{125}I]α-bgt sites on the surface of transfected human embryonic kidney (HEK) cells and ACh competition against the initial rate of [^{125}I]α-bgt binding were determined as described elsewhere (24). ACh competition measurements were analyzed using Hill equation: $1 - Y = 1/(1+([ACh]/K_{ov})^n)$, where Y is fractional occupancy by ACh, n is the Hill coefficient, K_{OV} is an overall dissociation constant.

Patch-clamp recordings and single-channel kinetic analysis. Recordings were obtained in the cell-attached configuration at a membrane potential of - 80 mV, at 22°C, and with bath and pipette solutions containing (mM): KCl 142, NaCl 5.4, $CaCl_2$ 1.8, $MgCl_2$ 1.7, HEPES 10, pH 7.4 (24). Single-channel currents were recorded using an Axopatch 200A amplifier (Axon Instruments) at a bandwidth of 50 kHz, digitized at 5 μs intervals using a Digidata 1322A (Axon Instruments), and recorded to hard disk using the program Clampex 8 (Axon Instruments). Records were analyzed at a uniform bandwidth of 11.7 kHz for recordings at ACh concentration of 50 nM and 10 kHz for recordings at 3 μM or above with TACx4.0.9 software (Bruxton). Dwell-time histograms were plotted on a logarithmic abscissa and fitted to the sum of exponentials by maximum likelihood (25).

To estimate rate constants underlying AChR activation, we employed desensitizing concentrations of ACh that cause events from a single channel to cluster into identifiable activation episodes (26). Clusters were identified as a series of closely spaced openings preceded and followed by closed intervals greater than a defined critical time. The critical time was determined by a method that misclassifies an equal number of events between two adjacent closed-time components (27). For each receptor, the critical time that provided the best fit for the

closed time histogram was chosen for the final analysis. Clusters with fewer than five openings were excluded from analysis. Individual clusters were examined for homogeneity by determining the mean open probability and open duration for each cluster, and clusters within two standard deviations of the means were accepted for further analysis (28, 29). The resulting global set of open and closed dwell times of wild-type and mutant AChRs were analyzed using the program MIL which uses an interval-based maximum likelihood method that also corrects for missed events (28). The kinetic analysis of wild-type and mutant receptors yielded a set of rate constants that were fitted to a scheme of receptor activation (see Figure 6 under Results).

For each type of AChR, single channel dwell times obtained over a range of ACh concentrations were fitted simultaneously. Data were obtained over a range of ACh concentrations from 10-300 μM for wild-type and αY127T/εL40P- AChR, from 100-1000 μM for αY127T- AChR, and from 3-1000 μM for other AChRs; 1,562-11,250 (mean 4,800) events were analyzed for each ACh concentration. The final set of rate constants were checked by superimposing probability density functions calculated from the rate constants on the experimental dwell time histograms, and by their ability to predict burst length at low ACh concentrations (30, 31).

Acknowledgments

This work was supported by NIH grants to A.G. Engel (NS-6277) and to S.M. Sine (NS-31744) and by a Muscular Dystrophy Association Grant to A.G. Engel. We thank Dr. Isabella Illa for patient referral.

Table 1. Morphometric analysis of endplate regions

Parameter	Patient	Controls
Nerve terminal area (μm^2)	3.28 ± 0.40	3.88 ± 0.39
	(27)	(63)
Postsynaptic area (μm^2)	6.13 ± 0.42[C]	10.60 ± 0.79
	(27)	(39)
Normalized postsynaptic membrane length	4.07 ± 0.20[C]	5.83 ± 0.25
($\mu m/\mu m^2$)[A]	(27)	(47)
Normalized AChR-reactive membrane	1.00 ± 0.13[C]	3.01 ± 0.11
length[B]	(16)	(85)

Values indicate mean ± SE; numbers in parentheses represent number of endplate regions. More than one region can occur at an endplate.

[A]Postsynaptic membrane length divided by postsynaptic area.

[B]AChR reactive postsynaptic membrane length divided by length of primary synaptic cleft.

[C]$P<0.001$

Table 2. In vitro microelectrode and α-bgt binding studies

	Patient	Controls
m^A	32 ± 5 (17)	31 ± 1 (190)
MEPP amplitude (mV)[B]	0.067 ± 0.011 (17)	1.00 ± 0.025 (165)
MEPC amplitude (nA)[C]	0.44 ± 0.064 (11)	3.95 ± 0.10 (79)
[^{125}I]α-bgt binding sites/EP	2.06 x 1E6	12.82 ± 0.79 E6 (13)

Values indicate mean ± SEM. Measurements at 29°C ± 0.5°C for MEPPs and EPPs recordings, and at 22°C ± 0.5°C for MEPCs recordings. Numbers in parenthesis indicate number of subjects for [^{125}I]α-bgt binding sites/EP and number of EPs for other measurements.

[A]Quantal content of EPP at 1 Hz stimulation corrected for a resting membrane potential of -80 mV, nonlinear summation, and non-Poisson release.

[B]Estimated by dividing the corrected EPP amplitude by *m*, and corrected for a fiber diameter of 50 μm.

[C]Estimated by dividing the EP current amplitude by *m*.

Table 3. Burst durations of wild-type and mutant AChRs in HEK cells

AChR	Burst (ms) $\tau_1(a_1)$	$\tau_2(a_2)$	$\tau_3(a_3)$
Wild-type	0.036 ± 0.002[A] (0.24 ± 0.02)	0.47 ± 0.06 (0.21 ± 0.03)	3.31 ± 0.12 (0.58 ± 0.04)
δL42P	0.18 ± 0.040 (0.69 ± 0.02)	0.76 ± 0.23 (0.31 ± 0.016)	
δV93L	0.12 ± 0.038[B] (0.14 ± 0.02)	1.41 ± 0.30 (0.4 ± 0.05)	4.83 ± 0.44 (0.52 ± 0.07)
δL42G	0.068 ± 0.011 (0.55 ± 0.06)	0.38 ± 0.02 (0.42 ± 0.08)	
δL42D	0.16 ± 0.024 (0.73 ± 0.04)	0.63 ± 0.31 (0.27 ± 0.04)	
δL42K	0.080 ± 0.009 (0.56 ± 0.03)	0.43 ± 0.02 (0.44 ± 0.03)	
εL40P	0.062 ± 0.01 (0.31 ± 0.03)	0.23 ± 0.04 (0.59 ± 0.03)	1.71 ± 0.14 (0.1 ± 0.008)
βL40P	0.48 ± 0.10 (0.50 ± 0.10)	2.27 ± 0.08 (0.50 ± 0.10)	
αL40P	0.11 ± 0.032 (0.22 ± 0.07)	1.67 ± 0.58 (0.41 ± 0.05)	12.98 ± 0.90 (0.36 ± 0.06)
δS40P	0.17 (0.23)	0.72 (0.53)	2.98 (0.24)
δN41P	0.074 ± 0.007 (0.37 ± 0.02)	0.61 ± 0.03 (0.63 ± 0.02)	
δI43P	0.030 ± 0.02 (0.24 ± 0.07)	0.69 ± 0.07 (0.76 ± 0.1)	
δS44P	0.024 ± 0.0007 (0.21 ± 0.04)	0.35 ± 0.03 (0.64 ± 0.04)	2.05 ± 0.54[C] (0.15 ± 0.03)

Twenty-one patches for wild-type, 5 for δV93L, 4 for βL40P and αL40P, multiple combined patches for δS40P, and 3 patches for all other AChRs were analyzed. Values indicate means ± SE. τ_n and a_n indicate time constants and fractional histogram areas. ACh = 50 nM; membrane potential = -80 mV; bandwidth = 11.7 kHz.

[A,B,C]not detected at 3, 2, and 1 patches, respectively.

Table 4. Activation kinetics of wild-type and mutant AChRs expressed in HEK cells

AChR	k_{+1}	k_{-1}	K_1 /μM	k_{+2}	k_{-2}	K_2 /μM	β_1	α_1	θ_1	β_2	α_2	θ_2	k_{+b}	k_{-b}	K_B /mM
Wild-Type	98 ±7	1,817 ±185	19	86 ±2	10,449 ±186	121	191 ±16	3,052 ±276	0.063	56,291 ±1,495	2,223 ±75	25	90 ±6	144,500 ±2,515	1.61
δL42P	193 ±51	139 ±66	0.7	96 ±6	6,072 ±362	63	438 ±37	6,919 ±334	0.063	6,772 ±146	3015 ±37	2	44 ±6	143,409 ±46,824	3.26
δL42G	101 ±29	115 ±48	1	153 ±7	10,525 ±502	69	111 ±12	11,149 ±760	0.010	4,741 ±85	3,978 ±39	1	7 ±1	58,093 ±4,344	8.30
δL42D	80 ±16	20 ±8	0.3	135 ±4	9,992 ±336	74	97 ±6	8,522 ±538	0.011	5,816 ±118	3,136 ±30	2	54 ±3	143,436 ±2,520	2.66
δL42K	671 ±63	4540 ±641	7	293 ±18	13,386 ±670	46	1489 ±168	18,085 ±727	0.082	13,076 ±312	6,065 ±113	2	7 ±1	71,284 ±8,194	10.18
εL40P	199 ±32	595 ±162	3	79 ±5	8,523 ±434	108	200 ±24	3,510 ±182	0.057	6,815 ±235	1,221 ±21	6	39 ±3	111,670 ±2,846	2.86
βL40P	229 ±33	1,313 ±207	6	159 ±7	21,706 ±754	137	ND	ND	ND	28239 ±1,197	1,106 ±30	26	13 ±2	103,260 ±7,671	7.94
αY127T	ND	ND	ND	ND	ND	ND	ND	ND	ND	182 ±2	3,568 ±46	0.051	14 ±1	66,021 ±3,060	4.72
αY127T+ δL42P	150 ±39	1,182 ±393	8	195 ±22	12,159 ±1,330	62	44 ±11	13,674 ±779	0.003	1,208 ±23	7,541 ±74	0.16	11 ±1	67,221 ±4,129	6.11
αY127T+ εL40P	ND	ND	ND	50 ±9	4,900 ±927	98	102 ±4	10,051 ±348	0.01	707 ±20	3,735 ±51	0.19	14 ±2	71,756 ±6,135	5.13
δL42P+ εL40P	ND	ND	ND	368 ±38	1,225 ±141	3	ND	ND	ND	885 ±11	5,965 ±53	0.15	9 ±1	61,364 ±5,848	6.82
αY127T+ δL42P+ εL40P	82 ±8	189 ±56	2	368 ±55	12,056 ±1,706	33	ND	ND	ND	1,823 ±45	8,462 ±104	0.22	6 ±1	45,991 ±8,050	7.67

Rate constants are in units per μM per sec for association rate constants, and per sec for all others. The dissociation constants, K_1, K_2 are the ratio of k_-/k_+. The channel gating equilibrium constants, θ_1, θ_2 are the ratios of the opening to closing rate constants, β_1/α_1, β_2/α_2, respectively.

Figure legends

Figure 1. EM localization of AChR with peroxidase labeled α-bgt at patient (A) and control (B) endplates. Bars = 1 μm.

Figure 2. Mutation analysis. (A) Multiple alignment of the β_1, β_2, and β_4 strands of AChR subunits. Leu 42 is conserved in all human ACR subunits and in δ subunits of all species. Note the δL42P, δI58K and δV93L in the β_1, β_2, and β_4 strand, respectively. (B) Family analysis.

Figure 3. α-Bungarotoxin binding studies. (A) [^{125}I]α-bgt binding to surface receptors on intact HEK cells transfected with the indicated AChR subunits. The results are normalized for α-bgt binding to wild-type AChR ($\alpha_2\beta\delta\varepsilon$) and represent mean and SD of three to six experiments. (B) Total α-bgt binding to saponin-permeabilized cells transfected with the indicated constructs. Amounts of bound [^{125}I]α-bgt are normalized to that measured for the wild-type dimer ($\alpha\delta$).

Figure 4. Single-channel events elicited by 50 nM ACh from HEK cells expressing wild-type and mutant AChRs. Left column: representative channel openings, shown as upward deflections. Right column: logarithmically binned burst duration histograms fitted to the sum of exponentials.

Figure 5. Activation kinetics of wild-type- and δL42P-AChR (A and B) and open channel probabilities (C). In (A) and (B), left column shows representative single-channel currents at indicated AChR concentrations recorded from HEK cells. Currents are shown as upward deflections; bandwidth 10 kHz. Center and right columns show corresponding histograms of closed and open durations with superimposed global fits for Scheme 1 for the entire range of

ACh concentrations. Fitted rate constants are shown in Table 4. (C) Open probability (P_{open}) as function of ACh concentration. Symbols and vertical lines indicate mean and standard deviation. Smooth curves represent functions predicted by the rate constants in Table 4.

Figure 6. Scheme of AChR activation.

Figure 7. Structural models of AChR (A and B) and mutant cycle analyses (C-F). Location of interacting residues on α and δ subunits in A with magnified view in B are shown on a structural model AChR generated with Torpedo AChR as template (Protein Data Bank code 2BG9). (C-F). In each mutant cycle, the coupling free energy ($\Delta\Delta G_{int}$) between the residues at upper right and low left corner was computed from $-RT\ln[(\theta_{ww}\theta_{mm})/(\theta_{wm}\theta_{mw})]$ (kcal/mol), where θ (β/α) is the gating equilibrium constant for diliganded receptors generated by kinetic fitting for wild-type (ww), single-mutant (wm, mw) or double-mutant (mm) receptors. Table 4 shows θ for each moiety of AChR. Free energy changes for channel gating are shown for each limb of the cycle. Traces above or below the indicated AChR constructs in panel C are representative single-channel currents at 100 μM ACh recorded from HEK cells. Currents are shown as upward deflections; bandwidth 10 kHz. Horizontal bar = 20 ms for wild-type and 100 ms for other moieties; vertical bar = 5 pA.

Figure 1

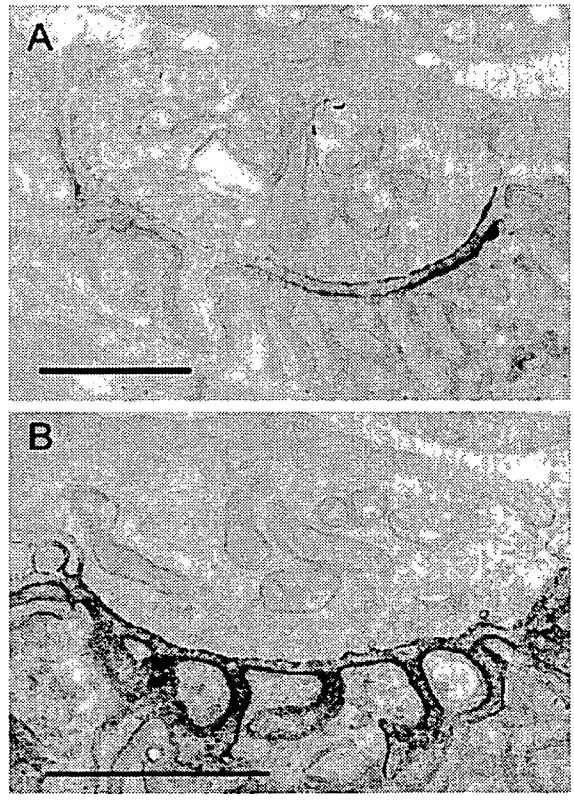

Figure 2

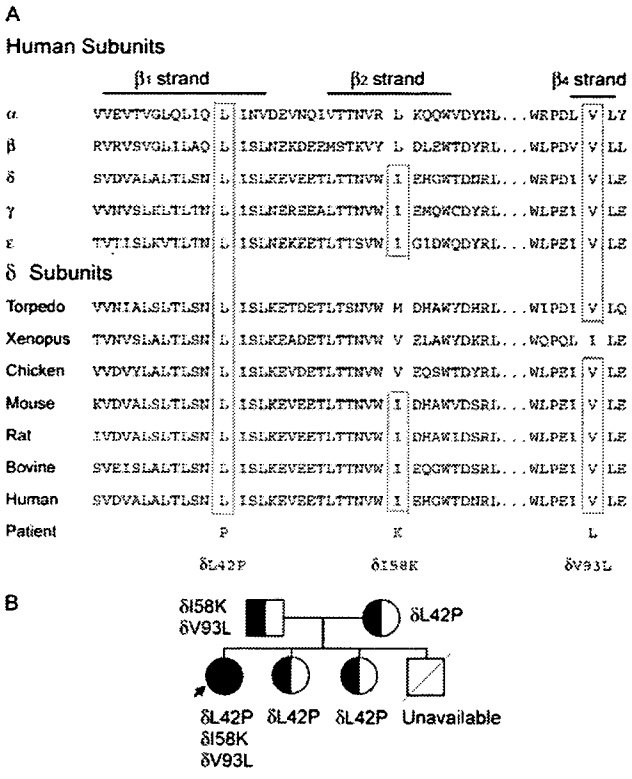
A
Human Subunits
β1 strand
β2 strand
β4 strand
α VVEVTVGLQLIQ L INVDEVNQIVTTNVR L KQQWVDYNL...WRPDL V LY
β RVRVSVGLILAQ L ISLNEKDEEMSTKVY L DLEWTDYRL...WLPDV V LL
δ SVDVALALTLSN L ISLKEVEETLTTNVW I EHGWTDDRL...WRPDI V LE
γ VVNVSLELTLTN L ISLNEREEALTTNVW I EMQWCDYRL...WLPEI V LE
ε TVTISLKVTLTN L ISLNEKEETLTTSVW I GIDWQDYRL...WLPEI V LE
δ Subunits
Torpedo VVNIALSLTLSN L ISLKETDETLTSNVW M DHAWYDHRL...WIPDI V LQ
Xenopus TVNVSLALTLSN L ISLKEADETLTTNVW V ELAWYDKRL...WQPQL I LE
Chicken VVDVYLALTLSN L ISLKEVDETLTTNVW V EQSWTDYRL...WLPEI V LE
Mouse KVDVALSLTLSN L ISLKEVEETLTTNVW I DHAWVDSRL...WLPEI V LE
Rat IVDVALSLTLSN L ISLKEVEETLTTNVW I DHAWIDSRL...WLPEI V LE
Bovine SVEISLALTLSN L ISLKEVEETLTTNVW I EQGWTDSRL...WLPEI V LE
Human SVDVALALTLSN L ISLKEVEETLTTNVW I EHGWTDNRL...WLPEI V LE
Patient P K L
δL42P δI58K δV93L
B
δI58K
δV93L
δL42P
δL42P δL42P δL42P Unavailable
δI58K
δV93L

Figure 3

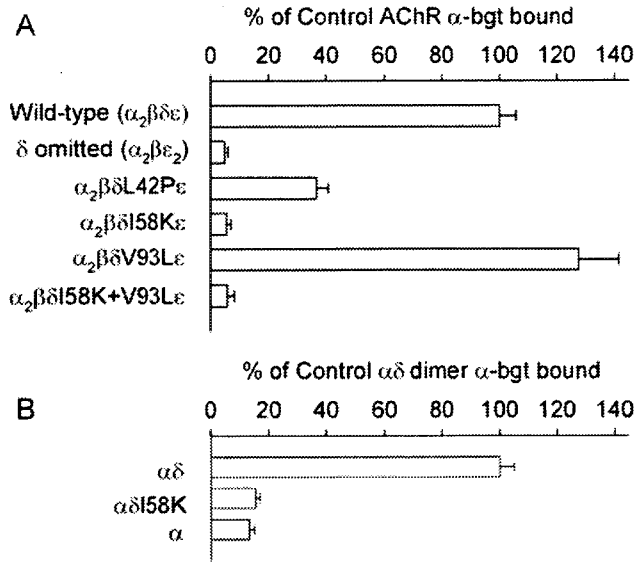
A
% of Control AChR α-bgt bound
0 20 40 60 80 100 120 140
Wild-type (α2βδε)
δ omitted (α2βε2)
α2βδL42Pε
α2βδI58Kε
α2βδV93Lε
α2βδI58K+V93Lε
B
% of Control αδ dimer α-bgt bound
0 20 40 60 80 100 120 140
αδ
αδI58K
α